IOP Publishing Modelling and Simulation in Materials Science and Engineering
Modelling Simul. Mater. Sci. Eng. **30** (2022) 074001 (15pp) https://doi.org/10.1088/1361-651X/ac8698

Modeling of microscale internal stresses in additively manufactured stainless steel

Yin Zhang[1,6], Kunqing Ding[1,6], Yejun Gu[2,3], Wen Chen[4], Y Morris Wang[5], Jaafar El-Awady[3], David L McDowell[1] and Ting Zhu[1,*]

[1] George W. Woodruff School of Mechanical Engineering, Georgia Institute of Technology, Atlanta, GA 30332, United States of America
[2] Institute of High Performance Computing, A*STAR, Fusionopolis, 138632, Singapore
[3] Department of Mechanical Engineering, Whiting School of Engineering, Johns Hopkins University, Baltimore, MD 21218, United States of America
[4] Department of Mechanical and Industrial Engineering, University of Massachusetts, Amherst, MA 01003, United States of America
[5] Department of Materials Science and Engineering, University of California, Los Angeles, CA 90095, United States of America

E-mail: ting.zhu@me.gatech.edu

Received 4 April 2022, revised 23 July 2022
Accepted for publication 3 August 2022
Published 24 August 2022

Abstract

Additively manufactured (AM) metallic materials often comprise as-printed dislocation cells inside grains. These dislocation cells can give rise to substantial microscale internal stresses in both initial undeformed and plastically deformed samples, thereby affecting the mechanical properties of AM metallic materials. Here we develop models of microscale internal stresses in AM stainless steel by focusing on their back stress components. Three sources of microscale back stresses are considered, including the printing and deformation-induced back stresses associated with as-printed dislocation cells as well as the deformation-induced back stresses associated with grain boundaries. We use a three-dimensional discrete dislocation dynamics model to demonstrate the manifestation of printing-induced back stresses. We adopt a dislocation pile-up model to evaluate the deformation-induced back stresses associated with as-printed dislocation cells. The extracted back stress relation from the pile-up model is incorporated into a crystal plasticity (CP) model that accounts for the other two sources of back stresses as well. The CP finite element simulation results agree with the experimentally measured tension–compression asymmetry and macroscopic back stress, the latter of which represents the effective resultant

*Author to whom any correspondence should be addressed.
[6]These authors contributed equally to this work.

of microscale back stresses of different origins. Our results provide an in-depth understanding of the origins and evolution of microscale internal stresses in AM metallic materials.

Keywords: additive manufacturing, internal stresses, crystal plasticity

(Some figures may appear in colour only in the online journal)

1. Introduction

Additively manufactured (AM) alloys often exhibit unconventional microstructures compared to their counterparts produced by traditional metallurgical routes [1–3]. For example, the extreme processing conditions of additive manufacturing by laser powder bed fusion (LPBF) lead to large temperature gradients and rapid cooling that can result in highly non-equilibrium microstructures such as solidification cells inside grains [2, 4]. The chemical composition in cell walls is different from that in cell interiors. Sometimes cell walls are decorated with oxide nanoprecipitates. As a result, the cell walls can trap dislocations and serve as a scaffold to form 'as-printed dislocation cells' [5, 6]. Similar as-printed dislocation structures are also observed in AM metals [7, 8] and alloys without chemical cells [9]. These as-printed dislocation cells and structures hinder dislocation glide during plastic deformation, thereby affecting the mechanical properties of AM metallic materials [9, 10].

The mechanics of as-printed dislocation structures has been studied in terms of microscale internal stresses [9], which refer to the microscopically inhomogeneous stress distribution inside a material. The internal stress is sometimes called the residual stress in the literature [11]. Here we use the term 'internal stress' instead of 'residual stress', considering that the internal stress not only arises in as-printed samples without loading, but also evolves with plastic deformation under loading [12]. Generally, the microscale internal stresses are classified as belonging to two major types: intergranular and intragranular stresses [13]. The intergranular internal stresses result from strain incompatibility between grains, and they self-equilibrate over a length scale of multiple grains. In contrast, the intragranular internal stresses arise from the dislocation structures and associated geometrically necessary dislocations (GNDs) inside grains. These GNDs produce long-range, directional internal stresses that self-equilibrate over cells via constituent back and forward stresses, giving rise to the kinematic hardening and Bauschinger effects [14–18]. The internal stresses can be characterized in terms of their effect on plastic flow and work hardening processes through a macroscopic back stress, which is the effective resultant of various microscale back stresses stemming from different types of structural heterogeneity [17]. The macroscopic back stress can be experimentally measured from the unloading branch of the stress–strain curve using the Dickson's method [19].

Recently, Chen *et al* [9] conducted an experimental study of microscale internal stresses in AM 316L austenitic stainless steel. The measured 0.2% offset yield strength was around 540 MPa, which is two to three times that of as-cast/wrought stainless steel. In particular, they measured a pronounced difference in tensile and compressive yield strengths, and indicated that such a tension–compression asymmetry was governed by the back stresses associated with printing-induced dislocation structures. They also measured substantial macroscopic back stresses during loading and attributed the major source of these back stresses to the deformation-induced dislocation structures. To enable an in-depth understanding of these experimental results, here we develop models to account for different sources of microscale back stresses in AM 316L stainless steel. Our three-dimensional (3D) discrete dislocation dynamics (DDD), dislocation pile-up, and crystal plasticity finite element (CPFE) simulations

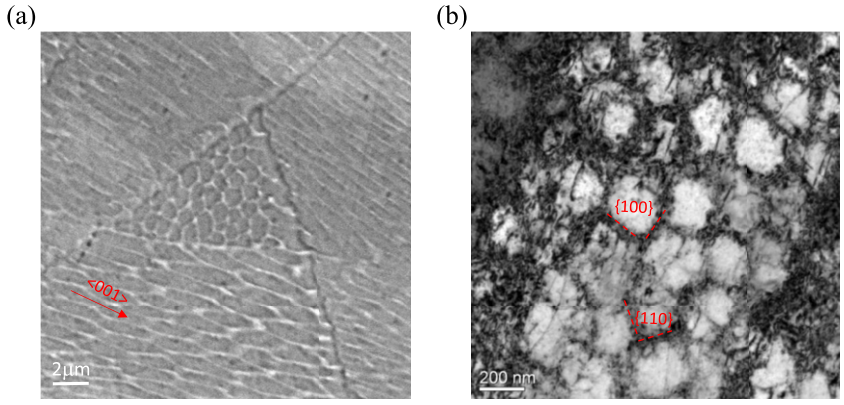

Figure 1. Coincident chemical cells and dislocation cells in as-printed 316L stainless steel processed using LPBF. (a) SEM image of domains of chemical cells elongated with different orientations. The red arrow indicates that the local cells elongate along an in-plane $\langle 001 \rangle$ direction. (b) TEM image of dislocation cells. The red dashed lines indicate that the cell walls are close to $\{100\}$ and $\{110\}$.

capture these microscale internal stresses in the form of back and forward stresses associated with dislocation structures and grain boundaries (GBs). The CPFE results are compared with the macroscopic back stress and tension–compression asymmetry from experimental measurements. Our work provides mechanistic insights into the origins and evolution of microscale internal stresses in AM metallic materials.

2. Internal stresses in as-printed dislocation cells

Figure 1(a) displays a scanning electron microscopy (SEM) image of an as-printed sample of 316L stainless steel processed using LPBF, which consists of domains of sub-grain chemical cells with different orientations. The sample was fabricated by a Concept M2 cusing machine, with a beam size of 54 μm, laser power = 150 W, scan speed = 700 mm s^{-1}, and build layer thickness = 30 μm. Within each domain, the chemical cells are elongated along a $\langle 001 \rangle$ direction, with the corresponding side walls parallel to $\{100\}$ or $\{110\}$. The middle triangle-shaped domain in figure 1(a) shows the $\langle 100 \rangle$ cross section of chemical cells that are approximately equiaxed. It is seen from this cross section that the cell size is on the order of ∼0.5 μm and the cell wall thickness is ∼0.1 μm. These chemical cells form because of constitutional supercooling and solute atom redistribution during cellular solidification [20], resulting in the Mo and Cr-rich cell walls. They coincide with dislocation cells (figure 1(b)), since the Mo and Cr-rich cell walls tend to trap dislocations and thus serve as a scaffold to the formation of 'as-printed dislocation cells'.

The as-printed dislocation cells result in a non-uniform distribution of microscale internal stresses across these cells. In general, the distribution of microscale internal stress in dislocation cells can be characterized through spatially resolved x-ray micro-diffraction measurement and DDD simulation. In this work, we use 3D DDD simulations to analyze the internal stress distribution in as-printed dislocation cells. Based on TEM observations, the simulated dislocation cell is assumed to form a rectangle box-shaped structure with cell walls parallel to the [100] (x-axis), [010] (y-axis) and [001] (z-axis) direction. Periodic boundary conditions are applied along all three directions. Figures 2(a) and (b) show the 3D and two-dimensional (2D)

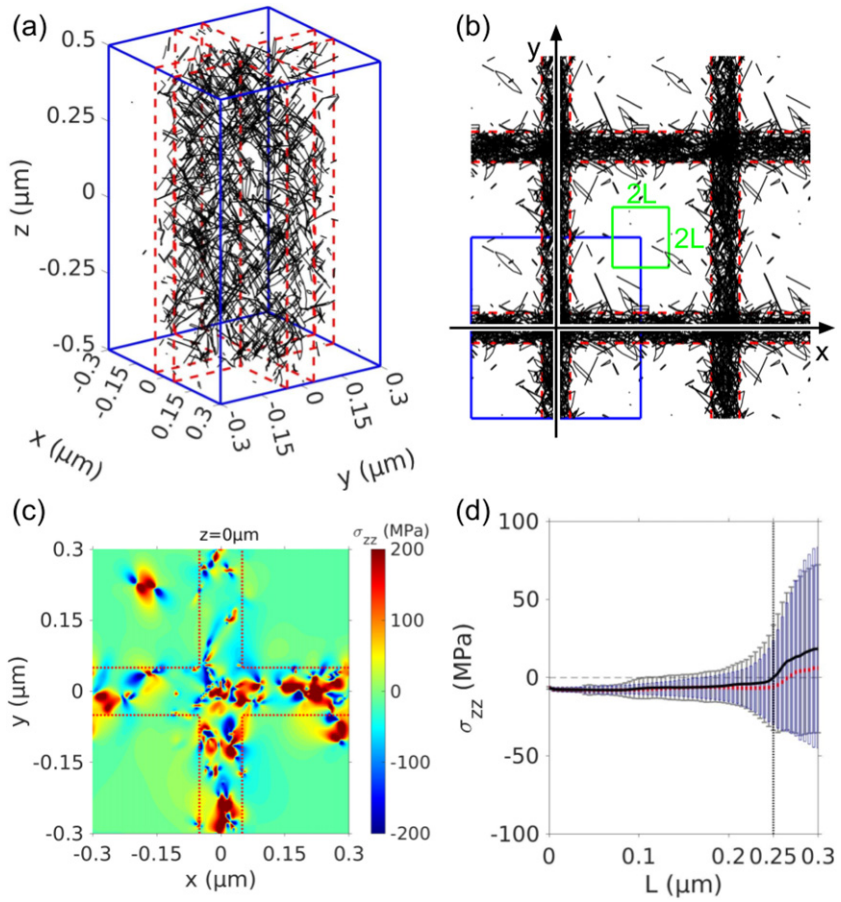

Figure 2. 3D DDD simulation results of internal stresses in a periodic volume containing idealized as-printed dislocation cells. (a) A representative 3D DDD simulation volume for the case with a cell wall dislocation density of 2×10^{15} m^{-2}, with periodic boundary conditions in all directions, containing two intersecting fully relaxed dislocation cell walls. (b) 2D view of the 3D cell structure in (a). The red dashed lines in (a) and (b) indicate the boundaries of the high dislocation density walls, while the blue box in (b) corresponds to the top view of the unit cell shown in (a). The green square in (b) represents the definition of the Chebyshev distance L to the center of the interior region. (c) Contour of σ_{zz} on the $z = 0$ plane of the cell structure in (a). (d) Distribution of σ_{zz} as a function of L through the entire 3D simulation cell of the structure in (a).

view of a unit dislocation cell structure containing two intersecting walls of high-density dislocations, respectively. The dimensions of the simulation domain are 0.6 μm × 0.6 μm × 1 μm in the x-, y-, and z-directions, respectively. Initially, rectangular dislocation edge dipolar loops (i.e., all segments are $\pm 3^\circ$ from the edge orientation) are randomly distributed in the simulation domain with the following conditions: (1) the dislocation density varies from 10^{15} to 10^{16} m^{-2} in the cell walls, with the dislocation density in the cell interior being 1%–2% of that in the cell walls [4]; (2) the dipole heights in the walls vary between 2 nm and 6 nm; and (3) the aspect ratio of the loops varies between 1/15 and 1/10. A 3D DDD simulation is performed to fully relax the dislocation cell structure without loading.

After the dislocation cell structure is fully relaxed (see figures 2(a) and (b)), the internal stress distribution across the dislocation cell is analyzed. Figure 2(c) shows a representative contour plot of the stress component σ_{zz} on the plane of $z = 0$ for the case with a cell wall dislocation density 2×10^{15} m^{-2}. It is observed that the cell walls exhibit higher stresses that vary markedly, whereas the cell interiors lower stresses that vary gently. To further characterize these internal stresses along the z-direction of the cell channel, σ_{zz} is expressed as a function of the Chebyshev distance. Namely, the Chebyshev distance of a point, L, is defined as the maximum value of the x-distance and y-distance to the center of the cell interior. Geometrically, the point (x_0, y_0, z_0) is on a square at the $z = z_0$ plane having an edge length of $2L$ whose center coincides with that of the cell interior, as illustrated in figure 2(c). Due to the periodicity of the cell structure, we have $0 \leqslant L \leqslant 0.3$ μm. The points with $L \leqslant 0.25$ μm are all in the cell interior and those with $L > 0.25$ μm are in the cell wall, and σ_{zz} as a function of L is plotted in figure 2(d). The three horizontal lines in each boxplot (blue vertical lines) from the bottom to the top display the 25th, 50th (median) and 75th percentiles of σ_{zz}. In addition, the grey error bar represents one standard deviation and the solid black line shows the average values. As such, figure 2(d) shows that the cell interior is on average under compression in the z-direction along the cell channel, while the cell wall is under tension; the corresponding average values of σ_{zz} in the cell interior and the cell wall are 5.28 MPa and −12.84 MPa, respectively.

Additional 3D DDD simulations with different initial dislocation densities and structures were carried out, while maintaining the same cell structure geometry and dimension. Figure 3 shows the internal stresses averaged along the z-direction as a function of L in different cases. It is seen that the cell interiors and walls have an opposite stress state: when the cell interior is under tension, the cell wall is under compression, and vice versa. Note that cases with the same cell wall dislocation density can have opposite internal stress distributions. This can be attributed to the different eigenstrains induced by different dislocation types used: vacancy dislocation loops (i.e., absence of a patch of atoms in a loop) usually result in an average tensile stress in the cell walls. In contrast, interstitial dislocation loops (i.e., addition of an extra patch of atoms in a loop) induce in an average compressive stress in the cell walls. A systematic study of the relationship between internal stresses and dislocation distributions will be presented in a follow-up paper.

The above 3D DDD results reveal the non-uniform distributions of microscale internal stresses across dislocation cells without loading, which exhibit several salient features. That is, the average internal stresses in the cell interiors and walls have opposite signs, as dictated by the self-equilibrium condition. The magnitudes of the average internal stresses in the cell walls are higher than those in the cell interiors, because of a typically lower volume fraction of the cell walls [4]. These internal stress characteristics provide support and insight for models of microscale internal stresses in AM stainless steel in section 3. We note that the internal stresses are dependent on the dislocation content in cell walls that is controlled by the complex thermomechanical history associated with large temperature gradients and rapid cooling during additive manufacturing [5, 6]. In order to enhance the capability of DDD simulations to better predict internal stresses in AM alloys, spatially resolved lattice strain measurements and detailed characterizations of dislocation microstructures are needed to calibrate the dislocation microstructures and internal stresses in DDD simulations in the future.

3. Modeling of back stresses in AM stainless steel

Previous studies in the literature [9, 10] and DDD simulations in section 2 indicate that the 'as-printed dislocation cells' in AM metallic materials can give rise to substantial microscale internal stresses in both initial undeformed and plastically deformed samples, thereby affecting

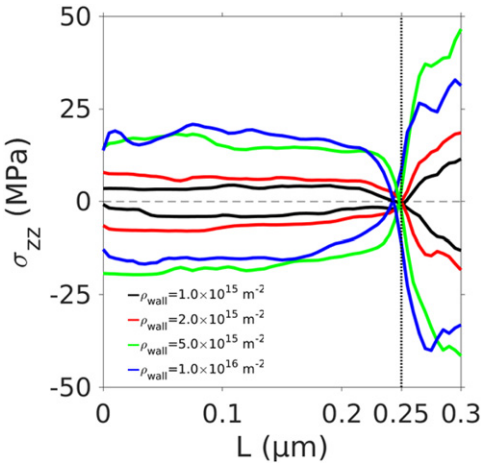

Figure 3. 3D DDD simulation results with different initial dislocation densities in cell walls ρ_{wall}.

the mechanical properties of these alloys. To gain an in-depth understanding of the mechanics of as-printed dislocation cells, we develop a crystal plasticity (CP) model that accounts for different sources of microscale internal stresses in AM 316L stainless steel by focusing on their back stress components. As schematically shown in figure 4(a), this CP model accounts for three sources of back stresses acting on a typical dislocation source such as a Frank–Read (FR) source inside a grain. These back stresses correspond to the long-range, directional stresses arising from GNDs associated with as-printed dislocation cells and GBs. Specifically, they include (1) the printing-induced back stresses (indicated by an orange arrow) from the GNDs at dislocation cell walls before loading, (2) the deformation-induced back stresses (indicated by a red arrow) from the GNDs (dislocation pile-ups) in as-printed dislocation cells, and (3) the deformation-induced back stresses (indicated by a pink arrow) from the GNDs at GBs. In section 3.1, we adopt a dislocation pile-up model to account for the evolution of deformation-induced back stresses in as-printed dislocation cells. The extracted back stress relation is incorporated into the CP model in section 3.2. This CP model accounts for all three sources of back stresses and is able to effectively represent the nonlinear evolution of these back stresses that dictates the macroscopic stress–strain response of AM stainless steel. This is shown by CPFE simulations of the macroscopic back stress and tension–compression asymmetry of AM 316L stainless steel in section 4.

3.1. Dislocation pile-up model

We adopt a dislocation pile-up model to account for the evolution of deformation-induced back stresses in as-printed dislocation cells. We follow Mughrabi's treatment of the dislocation cells as a composite material that is made of hard and soft components [21]. Namely, the cell walls and interiors are the hard and soft components that contain high and low densities of dislocations, respectively. The generation of directional internal stresses in the two components is considered to result from dislocation pile-ups due to the operation of dislocation sources such as FR sources in the cell interior. As illustrated in figure 4(b), a representative dislocation pile-up is under an applied shear stress and held against a cell wall. The dislocations in the pile-up collectively exert a back stress on the dislocation source. This back stress opposes the

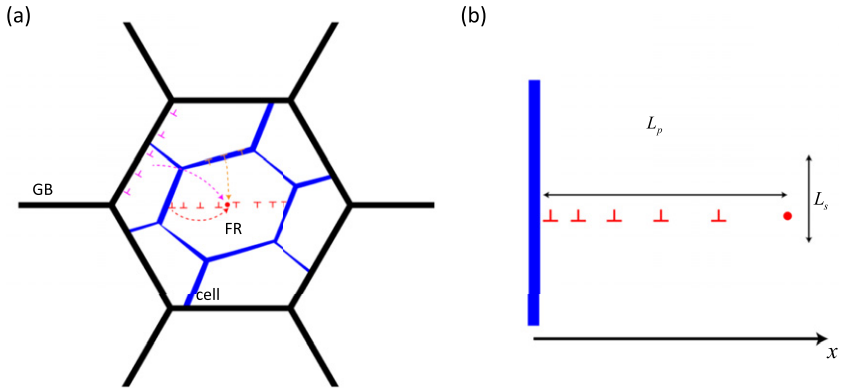

Figure 4. Schematic illustrations of multiple sources of back stresses. (a) Three sources of back stresses (indicated by colored arrows) acting on a typical dislocation source such as a Frank–Read (FR) source inside a grain (enclosed by GBs represented by black segments) containing as-printed dislocation cells enclosed by cell walls (blue segments). (b) A dislocation pile-up against a dislocation cell wall (thick blue line). The distance between the cell wall and the FR solution (red dot) is L_{p}, and the spacing between neighboring pile-ups on parallel slip planes is L_{s}.

applied stress and thus lowers the local stress acting on the dislocation source. Meanwhile, the dislocations in the pile-up collectively exert a forward stress to push against the cell wall. This forward stress aids the applied stress and thus raises the local stress acting on dislocation sources in the cell wall. To achieve self-equilibrium, the forward stress in the narrow cell wall is more intense than the back stress in the wide cell interior. With increasing load, both forward and back stresses rise in a running balance, thus elevating the microscale internal stresses associated with dislocation cells.

To formulate the dislocation pile-up model in figure 4(b), we consider a FR source located at a distance L_{p} from the cell wall, which corresponds to half of the dislocation cell size. The spacing between two neighboring pile-ups on parallel slip planes in a grain is L_{s}. This FR source has the critical operation stress s_{FR}. A non-uniform distribution of N_i dislocations in the pile-up collectively produce an internal shear stress at x by

$$\tau_i^{\mathrm{Cell}} = \sum_{j=1}^{N_i} \frac{\mu b}{2\pi(1-\nu)} \frac{1}{x - x_j} \tag{1}$$

where μ is the shear modulus, b is the Burgers vector length, ν is Poisson's ratio, and x_j is the equilibrium position of the jth dislocation given by the solution from Eshelby *et al* [22]. For a given N_i value, the applied shear stress τ_i and the back stress at the FR source $\tau_{b,i}^{\mathrm{Cell}} = \tau_i^{\mathrm{Cell}}(x = L_{\mathrm{p}})$ should satisfy

$$\tau_i - \tau_{b,i}^{\mathrm{Cell}} = s_{\mathrm{FR}} \tag{2}$$

meaning that the back stress acting on the FR source becomes sufficiently large to inhibit and eventually shut down its operation. From equations (1) and (2), $\tau_{b,i}^{\mathrm{Cell}}$ can be determined as a function of N_i. To incorporate the $\tau_{b,i}^{\mathrm{Cell}}$ vs N_i relation on a single slip system into the CP model accounting for multiple slip systems, we express $\tau_{b,i}^{\mathrm{Cell}}$ as

$$\tau_{b,i}^{\text{Cell}} = \alpha \frac{N_i \mu b}{L_{\text{p}}} \tag{3}$$

where α is a fitting parameter that is assumed to depend on s_{FR} only, as verified by our numerical results in section 4. In addition, the dislocation pile-up also exerts a forward stress $\tau_{\text{f},i}$ to the cell wall, which can be estimated from the stress acting on the leading dislocation by all other $N_i - 1$ dislocations in the pile-up. According to the solution of equilibrium dislocation positions in a pile-up from Eshelby *et al* [22], the forward stress can be expressed as

$$\tau_{f,i} = (N_i - 1)\tau_i. \tag{4}$$

3.2. Crystal plasticity model

Based on the back stress model on a single slip system in section 3.1, we develop a CP model to account for all three sources of back stresses in AM stainless steel. The CP constitutive equations are formulated within the rate-dependent, finite-strain framework of elastic-plastic deformation in crystal grains [23]. The deformation gradient tensor $\mathbf{F}$ within each grain is decomposed into the elastic deformation gradient tensor $\mathbf{F}^{\text{e}}$ and plastic deformation gradient tensor $\mathbf{F}^{\text{p}}$ by $\mathbf{F} = \mathbf{F}^{\text{e}}\mathbf{F}^{\text{p}}$. The elastic Green strain tensor is given by $\mathbf{E}^{\text{e}} = 1/2(\mathbf{F}^{\text{eT}}\mathbf{F}^{\text{e}} - \mathbf{I})$, where $\mathbf{I}$ is the second-order identity tensor. The second Piola–Kirchhoff stress $\mathbf{T}^*$ is given by $\mathbf{T}^* = \mathbf{C}\mathbf{E}^{\text{e}}$, where $\mathbf{C}$ is the fourth-order stiffness tensor for each grain. The rate of $\mathbf{F}^{\text{p}}$ is given by

$$\dot{\mathbf{F}}^{\text{p}} = \mathbf{L}^{\text{p}}\mathbf{F}^{\text{p}} \tag{5}$$

where $\mathbf{L}^{\text{p}}$ is the plastic velocity gradient tensor involving the superposition of the plastic shearing rate on 12 $\{111\}\langle 110\rangle$ slip systems in a face-centered cubic crystal

$$\mathbf{L}^{\text{p}} = \sum_{i=1}^{12} \dot{\gamma}_i^{\text{p}} \mathbf{m}_i \otimes \mathbf{n}_i \tag{6}$$

where $\dot{\gamma}_i^{\text{p}}$ is the plastic shear strain rate on the ith slip system, $\mathbf{m}_i$ and $\mathbf{n}_i$ are unit vectors of the associated slip plane normal and slip direction, and $\otimes$ stands for the outer product of two vectors. The plastic shearing rate is given by

$$\dot{\gamma}_i^{\text{p}} = \dot{\gamma}_0 \left(\frac{\left| \tau_i - \tau_{b,i}^{\text{Cell}} - \tau_{b,i}^{\text{GB}} - \tau_{b,i}^{\text{Pr}} \right|}{s_i} \right)^{\frac{1}{m_1}} \text{sgn}\left(\tau - \tau_{b,i}^{\text{Cell}} - \tau_{b,i}^{\text{GB}} - \tau_{b,i}^{\text{Pr}} \right) \tag{7}$$

where τ_i is the resolved shear stress on the ith slip system that is given approximately by $\tau_i = \mathbf{T}^* : \text{sym}(\mathbf{m}_i \otimes \mathbf{n}_i)$, $\dot{\gamma}_0$ is the reference plastic shearing rate, and m_1 is the strain rate sensitivity. In equation (7), s_i is the non-directional slip resistance associated with short-range obstacles that hinder dislocation glide; it has an identical initial value of s_0 for all slip systems and evolves as $\dot{s}_i = \sum_j h_{ij} \left| \dot{\gamma}_j^{\text{p}} \right|$ and $h_{ij} = q_{ij} h_0 (1 - s_j/s_{\text{sat}})^a$, where q_{ij} is the latent hardening matrix and the diagonal elements are 1.0 while the off-diagonal elements are 1.4. The hardening parameters h_0, a and s_{sat} are taken to be identical for all slip systems.

In equation (7), three sources of microscale back stresses $\tau_{b,i}^{\text{Cell}}$, $\tau_{b,i}^{\text{GB}}$ and $\tau_{b,i}^{\text{Pr}}$ are taken into account on each slip system. The $\tau_{b,i}^{\text{Cell}}$ term represents the back stress arising from deformation-induced GNDs associated with as-printed dislocation cells. According to the back stress relation given by the dislocation pile-up model in section 3.1, we express $\tau_{b,i}^{\text{Cell}}$ by rewriting equation (3) as

$$\tau_{b,i}^{\text{Cell}} = \alpha \mu \rho_i b L_{\text{s}} \tag{8}$$

In equation (8), ρ_i is the density of GNDs on the ith slip system, and it is related to N_i by $\rho_i = N_i/(L_s L_p)$. Likewise, we express the forward stress in the cell wall $\tau_{f,i}^{\text{Cell}}$ by rewriting equation (4). That is, considering N_i is proportional to τ_i, we rewrite $\tau_{f,i}^{\text{Cell}}$ as a second-order polynomial function of N_i.

$$\tau_{f,i}^{\text{Cell}} = \begin{cases} \left[a_0\left(\rho_i L_s L_p\right)^2 + b_0|\rho_i L_s L_p| + c_0\right]\text{sgn}(\rho_i L_s L_p) & \text{if } |\rho_i L_s L_p| > 1 \\ 0 & \text{if } |\rho_i L_s L_p| \leqslant 1 \end{cases} \tag{9}$$

where a_0, b_0 and c_0 are the parameters that are determined by fitting to the numerical result of $\tau_{f,i}^{\text{Cell}}$ as a function N_i from the pile-up model in section 3.1. The fitted forward stress is truncated at $N_i = 1$, below which there are no dislocations in the pile-up to exert the forward stress.

According to equation (8) and (9), the evolution of $\tau_{b,i}^{\text{Cell}}$ and $\tau_{f,i}^{\text{Cell}}$ with ρ_i reflects the competing effects of deformation-induced hardening and softening. These effects are respectively represented by the increase and decrease of ρ_i according to

$$\dot{\rho}_i = \dot{\rho}_i^{+} - \dot{\rho}_i^{-} \tag{10}$$

In equation (10), $\dot{\rho}_i^{+}$ is the rate of increase of dislocations in pile-ups due to the operation of FR sources in cell interiors. Following Mecking and Kocks [24], we express this hardening process by

$$\dot{\rho}_i^{+} = \frac{\dot{\gamma}_i^{\text{p}}}{bL_s} \tag{11}$$

In equation (10), $\dot{\rho}_i^{-}$ is the rate of decrease of dislocations in pile-ups due to plastic relaxation in cell walls. Such plastic relaxation is driven by the forward stresses in the cell walls, causing forest cutting and/or annihilation of dislocation dipoles therein [12]. As a result, the leading dislocations in the pile-ups penetrate into the cell walls, resulting in a decrease of dislocations in the pile-ups. We represent this softening process by

$$\dot{\rho}_i^{-} = C_\rho|\dot{\gamma}_i^{\text{p}}|\left(\frac{|\tau_i + \tau_{f,i}^{\text{Cell}}|}{s_w}\right)^{\frac{1}{m_2}}\text{sgn}(\rho_i) \tag{12}$$

where s_w is the resistance to plastic relaxation in the cell walls, C_ρ and m_2 are the fitting parameters.

Equations (8)–(12) represent the nonlinear evolution of the back stress arising from deformation-induced GNDs (through dislocation pile-ups) associated with as-printed dislocation cells. During the early stage of plastic deformation, both the back and forward stresses rise in a running balance. Since dislocation multiplication in the cell interiors dominates over plastic relaxation in the cell walls, $\dot{\rho}_i^{+}$ is greater than $\dot{\rho}_i^{-}$. As a result, both the back and forward stresses increase strongly with increasing ρ_i. During further plastic deformation, the increasing forward stress enhances plastic relaxation in the cell walls, leading to a stronger increase of $\dot{\rho}_i^{-}$ than $\dot{\rho}_i^{+}$ and eventually giving rise to a saturated $\tau_{b,i}^{\text{Cell}}$ at large plastic deformation.

The $\tau_{b,i}^{\text{GB}}$ term in equation (7) represents the back stress arising from the deformation-induced GNDs associated with GBs. Whereas a similar dislocation pile-up model as the one for $\tau_{b,i}^{\text{Cell}}$ can be used to represent the nonlinear evolution of $\tau_{b,i}^{\text{GB}}$, we adopt a simplified form by Armstrong and Frederick [25]

$$\dot{\tau}_{b,i}^{\text{GB}} = C_1\dot{\gamma}_i^{\text{p}} - C_2\tau_{b,i}^{\text{GB}}\left|\dot{\gamma}_i^{\text{p}}\right| \tag{13}$$

where C_1 is the hardening coefficient and C_2 is the recovery coefficient.

The $\tau_{b,i}^{\mathrm{Pr}}$ term in equation (7) represents the initial printing-induced back stress associated with dislocation cells in as-printed samples and thus does not evolve with plastic deformation. It has been previously shown that the printing-induced back stress is responsible for the tension–compression asymmetry of AM stainless steel [9]. Hence, it is necessary to include this back stress term in the CP model. However, it remains challenging to establish a functional relationship between $\tau_{b,i}^{\mathrm{Pr}}$ on individual slip systems and the complex thermal-mechanical history of a printing process. Hence, we assign a constant back stress tensor $\mathbf{B}_0$ for all the grains and calculate $\tau_{b,i}^{\mathrm{Cell}}$ by resolving $\mathbf{B}_0$ onto each slip system as

$$\tau_{b,i}^{\mathrm{Pr}} = \mathbf{B}_0 : (\mathbf{m}_i \otimes \mathbf{n}_i) \tag{14}$$

We assume the non-zero diagonal components to $\mathbf{B}_0$ and fit these components to the experimental result of tension–compression asymmetry. The above CP model takes account of different sources of back stresses associated with the printing and deformation-induced microscale internal stresses in AM stainless steel, and it can be generally applied to a broader range of AM metallic materials. The model is implemented in the general finite element package ABAQUS/Explicit [26] by writing a user material subroutine VUMAT.

4. Results and discussion

4.1. Internal stresses from a dislocation pile-up

To evaluate the back stress given by the dislocation pile-up model in section 3.1, we consider a range of applied resolved shear stresses τ_i when $L_{\mathrm{p}} = 0.5\mu\mathrm{m}$ and $s_{\mathrm{FR}} = 110$ MPa (giving the initial value s_0 for the slip resistance s_i in equation (7)). Based on equations (1) and (2), we calculate the equilibrium dislocation positions x_j ($j = 1 \ldots N_i$) in the pile-up under a given τ_i value, as shown in figure 5(a). Then we calculate the corresponding back stresses $\tau_i^{\mathrm{Cell}}(x = L_{\mathrm{p}})$ acting on the dislocation source using equation (1). As shown in figure 5(b), the calculated back stresses $\tau_{b,i}^{\mathrm{Cell}}$ (black line) against the number of dislocations N_i can be well fitted by the linear relation in equation (3) with the fitted dimensionless coefficient α of 1.455. This result indicates that $\tau_{b,i}^{\mathrm{Cell}}$ increases linearly with N_i in the pile-up. From the pairs of τ_i and N_i, we also calculate the corresponding forward stress using equation (4), as shown in figure 5(b) (red line). The calculated forward stress against N_i can also be fitted by the nonlinear relation in equation (9). The fitted parameters a_0, b_0 and c_0 are 21.57, 78.93 and -100.24 respectively.

4.2. Shear stress–strain response on a single slip system

To demonstrate the stress–strain response given by the CP model in section 3.2, we simulate the shear stress–strain response on a single slip system by including the back stress terms of $\tau_{b,i}^{\mathrm{Cell}}$ and $\tau_{b,i}^{\mathrm{GB}}$ in equation (7), while taking $\tau_{b,i}^{\mathrm{Pr}}$ as zero. The effect of nonzero $\tau_{b,i}^{\mathrm{Pr}}$ will be studied in section 4.3. This study allows us to track the evolution of the deformation-induced back stresses associated with both printing-induced dislocation cells and GBs in loading–unloading cycles. The initial value of the nondirectional slip resistance s_0 is taken as $s_{\mathrm{FR}} = 110$ MPa. Other parameters of s_i, $\tau_{b,i}^{\mathrm{Cell}}$ and $\tau_{b,i}^{\mathrm{GB}}$ are listed in table 1. We implement this simplified CP model for a single slip system by writing a Matlab program. Figure 6 shows the simulated shear stress–strain hysteresis loops from two strain-controlled load cycles. As observed from equation (14), τ_b^{GB} saturates when $\dot{\tau}_{b,i}^{\mathrm{GB}}$ becomes zero. Thus, the ratio of hardening and recovery coefficients C_1/C_2 determines the saturated value of τ_b^{GB}, which is taken as 74.1 MPa. Since the hardening coefficient C_1 is taken as a high value of 126 GPa, τ_b^{GB} dominates in the early

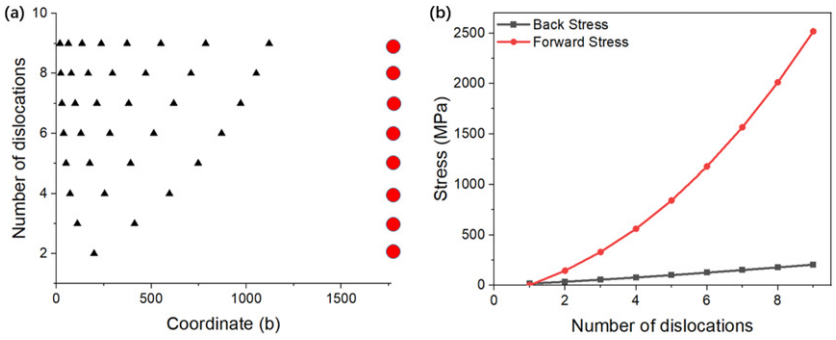

Figure 5. Numerical results of the dislocation pile-up model in figure 4(b). (a) Equilibrium dislocation positions x_j (black triangles) for a dislocation pile-up under different applied resolved shear stresses τ_i. For a given τ_i, the number of dislocations N_i in the pile-up is determined from equation (2) at the dislocation source (red dot). The dislocation positions x_j are normalized by the Burgers vector length b. (b) Back stress and forward stress are calculated as a function of the number of dislocations in the pile-up, respectively.

Table 1. Parameters used in single-slip and CP simulations.

$\dot{\gamma}_0$ (s^{-1})	s_0 (MPa)	h_0 (MPa)	s_{sat} (MPa)	a	μ (GPa)	m_1	L_p (μm)
0.001	110	320	447	0.7	126	0.02	0.5
L_s (μm)	s_w (MPa)	C_ρ (μm^{-2})	m_2	b (nm)	C_1 (GPa)	C_2	ν
0.5	3000	1.15×10^5	0.8	0.284	126	1700	0.3

stage of hardening response. On the other hand, $\tau_{b,i}^{\text{Cell}}$ represents the extra strengthening effect due to the deformation-induced storage of GNDs associated with as-printed dislocation cells. The increase of $\tau_{b,i}^{\text{Cell}}$ is less steep than $\dot{\tau}_{b,i}^{\text{GB}}$, and its saturation value is 40.3 MPa. Both $\tau_{b,i}^{\text{Cell}}$ and $\tau_{b,i}^{\text{GB}}$ become saturated at a strain level of ∼0.5%. Afterwards, the strain hardening response is controlled by the hardening effects of short-range obstacles to dislocation glide, as represented by a much lower rate of increase of s_i rather than the rates of increase of $\tau_{b,i}^{\text{Cell}}$ and $\tau_{b,i}^{\text{GB}}$ that have become saturated.

4.3. Crystal plasticity finite element results

We perform CPFE simulations of uniaxial tension and compression of AM stainless steel using the CP equations in section 3.2, which accounts for all three sources of back stresses given in equation (7). These CP equations are implemented in ABAQUS/Explicit [26] by writing a user material subroutine (VUMAT) with the material parameters in table 1. The finite element polycrystal model of AM stainless steel is taken as an assembly of 125 grains with random orientations. Each grain is represented by a brick element with reduced integration (C3D8R). As shown in our previous work [9], such type of polycrystal model can effectively capture the experimentally measured stress–strain behavior of AM stainless steel. To capture the tension–compression asymmetry, we assign the non-zero normal components and zero shear components of the printing-induced back stress tensor $\mathbf{B}_0$. The component along the build direction is 54 MPa and the components along the loading and transverse directions are

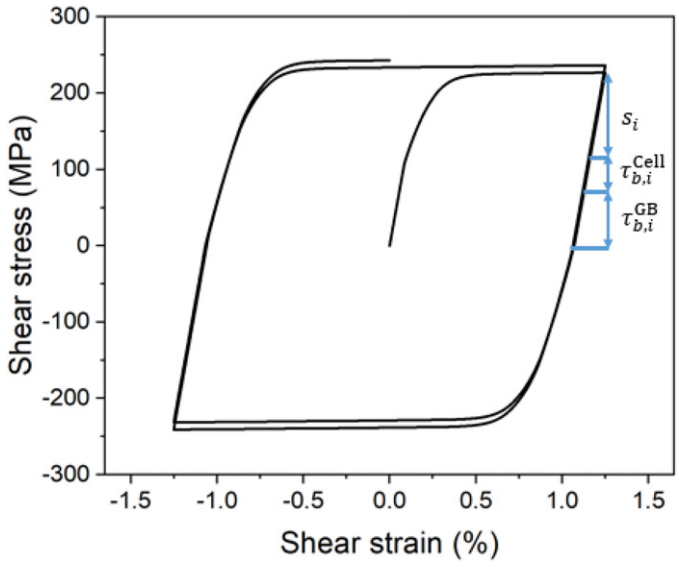

Figure 6. Simulated shear stress–strain hysteresis loops on a single slip system given by the simplified CP model that includes the back stress terms of $\tau_{b,i}^{\mathrm{Cell}}$ and $\tau_{b,i}^{\mathrm{GB}}$ in equation (7) by taking $\tau_{b,i}^{\mathrm{Pr}}$ as zero. The total flow stress of 226.8 MPa at the strain of 1% involves the contribution of s_i, $\tau_{b,i}^{\mathrm{Cell}}$ and $\tau_{b,i}^{\mathrm{GB}}$ by about 112.4 MPa, 40.3 MPa and 74.1 MPa, respectively.

-27 MPa. Compared to the case of vanishing $\mathbf{B}_0$, the compressive yield strength is raised by 27 MPa, while the tensile yield strength is reduced by 27 MPa. As a result, the printing-induced back stress $\mathbf{B}_0$ gives an asymmetry of tensile and compressive yield strength by 54 MPa. Figure 7(a) shows the CPFE results of uniaxial tensile and compressive stress–strain curves, which closely match the experimental results beyond the transient initial yield point region, including the tension–compression asymmetry. However, there exists a certain difference around the yield points in the tensile and compressive stress–strain curves between experiments and CPFE simulations, due to the limited nonlinearity of equation (13). This initial yielding region can be improved by enhancing the simplified form of the nonlinear evolution of $\tau_{b,i}^{\mathrm{GB}}$ in equation (13), if desired. The $\mathbf{B}_0$ values used are the fitting results for matching the experimental measurement and model prediction of the amount of asymmetry in tensile and compressive yield strengths. The physical origin of these back stresses associated with printing-induced dislocation structures in initial undeformed samples warrants further study in the future [27].

Figure 7(b) shows the magnified tensile loading-unloading curve around the tensile strain of 3%. From the unloading branch, the macroscopic back stress of the polycrystalline sample is determined as follows. The macroscopic back stress, σ_b, is given by $\sigma_b = (\sigma_0 + \sigma_u)/2$, where σ_0 is the flow stress prior to unloading, σ_u is the stress at the onset of reverse yielding, and the effective stress is $\sigma_{eff} = \sigma_0 - \sigma_b$. The $\sigma_b$value is determined as 420 MPa, given $\sigma_0 = 690$ MPa and $\sigma_u = 150$ MPa which are consistent with the experimental values [9].

Altogether, figure 7 demonstrates that our CP model can effectively account for different sources of back stresses and give predictions that closely match the macroscopic

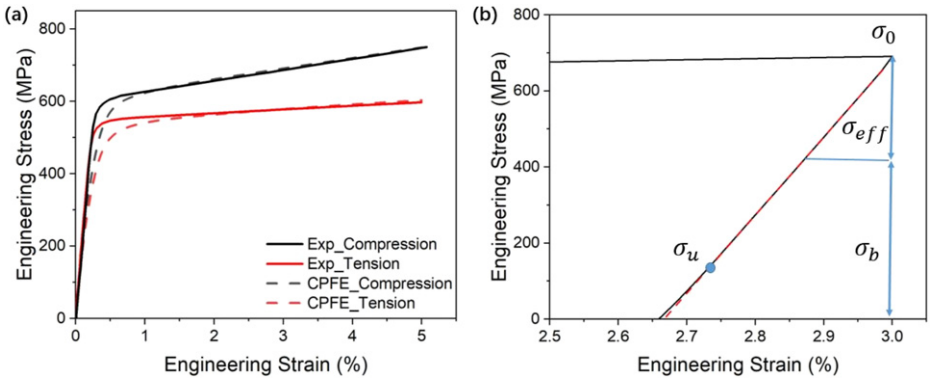

Figure 7. CPFE simulation results. (a) Comparison of stress–strain curves under uniaxial tension and compression between experiments [9] (solid lines) and CPFE simulations (dashed lines) for as-printed samples. (b) Determination of simulated back stress from an unloading branch using Dickson's method.

stress–strain behavior of AM stainless steel, including the macroscopic back stress and tension–compression asymmetry. Moreover, the CP model is informed by a dislocation pile-up model and thereby provides an in-depth understanding of how the deformation-induced back and forward stresses associated with as-printed dislocation cells affect the nonlinear stress–strain response of AM stainless steel at the macroscopic scale.

5. Concluding remarks

AM metallic materials often exhibit highly heterogeneous microstructures such as as-printed dislocation cells inside grains. In general, strong structural heterogeneity in a material gives rise to complex mechanical heterogeneity [12, 28, 29], which is manifested as multiple sources of microscale internal stresses. In this work, we develop models of microscale internal stresses originated from highly heterogeneous microstructures in AM stainless steel, and focus on their back stress components. These models connect the microscale internal stresses to the overall stress–strain response as well as the unique deformation characteristics such as the substantial macroscopic back stress and tension–compression of AM stainless steel. The necessity to include multiple sources of microscale back stresses for the constitutive modeling of AM metallic materials is underscored, and it is in line with a broad class of plasticity models that include multiple back stress terms [14–18]. In addition, the DDD simulation is used to demonstrate the manifestation of heterogeneous internal stresses in dislocation cell structures. It provides support and insight for the CPFE model that accounts for heterogeneous internal stresses in dislocation cell structures. Further studies are needed to bridge DDD and CPFE simulations through passing of quantitative information in the future.

Given the great potential of AM metallic materials for engineering applications, the mechanics of heterogeneous microstructures including as-printed dislocation structures warrants further studies in the future. For example, a combined experimental and modeling study is needed to characterize the relative contributions of different sources of microscale internal stresses to the macroscopic stress–strain response, including the macroscopic back stress. Furthermore, it is essential to correlate different sources of microscale back stresses with underlying dislocation microstructures. To this end, we note that recent years have witnessed rapid development of *in situ* characterization approaches through advanced x-ray microscopy

[30, 31], transmission electron microscopy [17], electron backscattered diffraction [8], etc. They enable high-resolution characterizations of the spatial-temporal evolution of dislocation distributions, lattice strains and orientations, etc. The integration between advanced *in situ* characterizations and constitutive models can open many opportunities to understand the effects of highly heterogeneous microstructures on the mechanical behavior of AM metals and alloys.

Acknowledgments

We thank A J Birnbaum and J G Michopoulos for insightful discussion on dislocation cells in AM alloys. TZ and DLM acknowledge support by the Office of Naval Research (N00014-18-1-2784). TZ acknowledges support by the National Science Foundation (DMR-2004412). YG and JAE acknowledge support by the Office of Naval Research (N00014-18-1-2858). WC and YMW acknowledge support by the National Science Foundation (DMR-2004429 and DMR-2104933, respectively).

Data availability statement

All data that support the findings of this study are included within the article (and any supplementary files).

ORCID iDs

Ting Zhu https://orcid.org/0000-0001-8612-9689

References

[1] DebRoy T *et al* 2018 *Prog. Mater. Sci.* **92** 112–224
[2] Wang Y M *et al* 2018 *Nat. Mater.* **17** 63–71
[3] Ren J *et al* 2022 *Nature* **608** 62–8
[4] Voisin T, Forien J-B, Perron A, Aubry S, Bertin N, Samanta A, Baker A and Wang Y M 2021 *Acta Mater.* **203** 116476
[5] Birnbaum A J, Steuben J C, Barrick E J, Iliopoulos A P and Michopoulos J G 2019 *Addit. Manuf.* **29** 100784
[6] Sudmanns M, Birnbaum A J, Gu Y, Iliopoulos A P, Callahan P G, Michopoulos J G and El-Awady J A 2022 *Addit. Manuf.* **55** 102791
[7] Li Z *et al* 2021 *Mater. Today* **50** 79–88
[8] Witzen W A, Polonsky A T, Rottmann P F, Pusch K M, Echlin M P, Pollock T M and Beyerlein I J 2022 *J. Mater. Sci.* **57** 9885–902
[9] Chen W, Voisin T, Zhang Y, Forien J-B, Spadaccini C M, McDowell D L, Zhu T and Wang Y M 2019 *Nat. Commun.* **10** 4338
[10] Ding K, Zhang Y, Birnbaum A J, Michopoulos J G, McDowell D L and Zhu T 2021 *Extreme Mech. Lett.* **49** 101503
[11] Hu J, Chen B, Smith D J, Flewitt P E J and Cocks A C F 2016 *Int. J. Plast.* **84** 203–23
[12] Cottrell A H 2002 Commentary. A brief view of work hardening *Dislocations in Solids* ed F R N Nabarro and M S Duesbery (Amsterdam: Elsevier) pp 7–17
[13] Dye D, Stone H J and Reed R C 2001 *Curr. Opin. Solid State Mater. Sci.* **5** 31–7
[14] Chaboche J L 1991 *Int. J. Plast.* **7** 661–78
[15] Feaugas X 1999 *Acta Mater.* **47** 3617–32
[16] Pham M S, Holdsworth S R, Janssens K G F and Mazza E 2013 *Int. J. Plast.* **47** 143–64

[17] Cheng Z, Bu L, Zhang Y, Wu H, Zhu T, Gao H and Lu L 2022 *Proc. Natl Acad. Sci. USA* **119** e2116808119
[18] Zirkle T, Zhu T and McDowell D L 2021 *Int. J. Plast.* **146** 103082
[19] Dickson J I, Boutin J and Handfield L 1984 *Mater. Sci. Eng.* **64** L7–L11
[20] Prashanth K G and Eckert J 2017 *J. Alloys Compd.* **707** 27–34
[21] Mughrabi H 1983 *Acta Metall.* **31** 1367–79
[22] Eshelby J D, Frank F C and Nabarro F R N 1951 *London, Edinburgh Dublin Phil. Mag. J. Sci.* **42** 351–64
[23] Kalidindi S R, Bronkhorst C A and Anand L 1992 *J. Mech. Phys. Solids* **40** 537–69
[24] Mecking H and Kocks U F 1981 *Acta Metall.* **29** 1865–75
[25] Armstrong P J and Frederick C 1966 A mathematical representation of the multiaxial Bauschinger effect *CEGB Report RD/B/N731* (Berkeley Nuclear Laboratories)
[26] ABAQUS/Explicit, 2009 User's Manual Version 6.9 (Providence, RI: Dassault Systems Simulia Corporation)
[27] Lindroos M, Pinomaa T, Ammar K, Laukkanen A, Provatas N and Forest S 2022 *Int. J. Plast.* **148** 103139
[28] Ma E and Zhu T 2017 *Mater. Today* **20** 323–31
[29] Zhu Y *et al* 2021 *Mater. Res. Lett.* **9** 1–31
[30] Simons H *et al* 2015 *Nat. Commun.* **6** 6098
[31] Li R *et al* 2018 *Proc. Natl Acad. Sci. USA* **115** 483–8